ADVANCED ENERGY & SUSTAINABILITY RESEARCH
www.advenergysustres.com

Toward Sustainable, High-Performance, and Scalable On-Chip Biopower: Microbial Biobatteries with 3D-Printed Stainless Steel Anodes and Spore-Based Biocatalysts

*Anwar Elhadad, Yang Gao, Guangfa Li, Jiaqi Yang, Dehao Liu, and Seokheun Choi**

The rapid proliferation of the Internet of Things (IoT) necessitates compact, sustainable, and autonomous energy sources for distributed electronic devices. Microbial fuel cells (MFCs) offer an eco-friendly alternative by converting organic matter into electrical energy using living micro-organisms. However, their integration into microsystems faces significant challenges, including incompatibility with microfabrication, fragile anode materials, low electrical conductivity, and compromised microbial viability. Here, this study introduces a microscale biobattery platform integrating laser powder bed fusion-fabricated 316L stainless steel anodes with resilient, spore-forming *Bacillus subtilis* biocatalysts. The 3D-printed gyroid scaffolds provide high surface-to-volume ratios, submillimeter porosity, and tunable roughness, enhancing microbial colonization and electron transfer. The stainless steel ensures mechanical robustness, chemical stability, and superior conductivity. *Bacillus subtilis* spores withstand harsh conditions, enabling prolonged storage and rapid, on-demand activation. The biobattery produces 130 μW of power, exceeding conventional microscale MFCs, with exceptional reuse stability. A stack of six biobatteries achieves nearly 1 mW, successfully powering a 3.2-inch thin-film transistor liquid crystal display via capacitor-assisted energy buffering, demonstrating practical applicability. This scalable, biologically resilient, and fabrication-compatible solution advances autonomous electronic systems for IoT applications.

1. Introduction

The accelerating proliferation of the Internet of Things (IoT) is fundamentally reshaping expectations placed on electronic hardware, with forecasts predicting cumulative production exceeding one trillion connected devices by 2035.[1,2] Many of these devices are embedded within challenging or disposable applications, such as smart packaging, biomedical implants, and structural-health monitoring sensors.[3] Powering this immense scale with conventional lithium-ion batteries would necessitate a massive global logistics infrastructure for frequent battery replacements, generating unsustainable hazardous waste and perpetuating energy-intensive manufacturing practices.[1] Although alternative methods like far-field wireless power transfer appear promising, their practicality remains severely limited by rapid power attenuation with distance and regulatory restrictions, prompting an urgent need for self-sustainable, microscale energy harvesters.[1,4]

Microbial fuel cells (MFCs), functioning as rechargeable biobatteries powered by renewable resources, uniquely address these needs.[4,5] Electrogenic microbial biofilms oxidize organic matter, ranging from wastewater to physiological fluids, and transfer the generated electrons to external circuits. These living biocatalysts naturally self-assemble, self-repair, and adapt dynamically to fluctuating environmental conditions, offering operational lifetimes that significantly exceed those of conventional electrochemical energy storage systems.[5,6] Recent developments in ultralow-power mixed-signal chipsets, achieving quiescent currents below nanowatt levels, have positioned the power demands of real-time sensing and intermittent telemetry well within the operational range

A. Elhadad, Y. Gao, S. Choi
Bioelectronics & Microsystems Laboratory
Department of Electrical & Computer Engineering
State University of New York at Binghamton
Binghamton 13902, New York, USA
E-mail: sechoi@binghamton.edu

The ORCID identification number(s) for the author(s) of this article can be found under https://doi.org/10.1002/aesr.202500199.

DOI: 10.1002/aesr.202500199

G. Li, J. Yang, D. Liu
Intelligent Manufacturing & Materials Design Lab
Department of Mechanical Engineering
State University of New York at Binghamton
Binghamton 13902, New York, USA

S. Choi
Center for Research in Advanced Sensing Technologies & Environmental Sustainability
State University of New York at Binghamton
Binghamton 13902, New York, USA

of microscale MFCs.[7] Nevertheless, integrating these promising concepts into practical microelectronic systems has stalled, predominantly due to severe constraints at the anode interface.[8–10] Achieving efficient electron harvesting from microbial metabolism at microscale dimensions involves overcoming multiple simultaneous challenges: ensuring adequate nutrient diffusion, efficient waste removal, mechanical robustness, high electrical conductivity, compatibility with standard microfabrication processes, and sustained microbial viability during harsh fabrication and storage conditions.[11–15]

Early efforts in micro-MFCs employed planar thin-film anodes patterned through photolithography.[16–20] However, their smooth surfaces severely limited biofilm formation, necessitating toxic mediators to enable electron transfer. Carbon-based 3D-printed anodes using techniques such as direct-ink writing and fused deposition modeling provided improved surface areas[21–26] but encountered significant drawbacks, including low electrical conductivity, structural fragility, and incompatibility with complementary metal-oxide-semiconductor (CMOS) integration due to high-temperature postprocessing requirements.[27] Additionally, microbial biobatteries inherently rely on living organisms incompatible with harsh, conventional microfabrication processes and cleanroom environments, further restricting their practical integration.[28,29] Addressing these multifaceted challenges demands innovative anode materials and specialized fabrication strategies uniquely tailored to biological compatibility. Stainless steel has emerged as a compelling candidate due to its exceptional electrical conductivity ($\approx 1.4 \times 10^6$ S m^{-1}), superior mechanical strength, chemical inertness, global availability, recyclability, and established performance in macroscale MFC applications.[30–32] The advent of laser powder bed fusion (LPBF) technology now facilitates precise, high-resolution 3D printing of stainless steel microarchitectures, achieving feature dimensions below 50 μm.[33,34] These LPBF-fabricated stainless steel lattices offer high porosity, mechanical robustness, and precisely tunable surface roughness, significantly enhancing microbial attachment, biofilm stability, and nutrient exchange capabilities essential for effective electron transfer in microscale bioelectrochemical systems. Bacterial endospores, robust dormant forms of certain bacteria, present significant potential for integration into microbial bioelectrochemical systems due to their exceptional resilience under extreme environmental conditions.[28,29] Endospores can remain dormant indefinitely, surviving harsh stresses such as heat, desiccation, and chemical exposure, and rapidly activate into metabolically active vegetative cells when favorable conditions return.[35,36] Studies have demonstrated endospore viability over extended periods, highlighting their suitability for long-term storage and reliable performance within microscale fabrication environments, thus making them particularly promising for practical MFC applications.[28,29,37–40]

This work reports the first successful integration of LPBF-fabricated 316L stainless steel gyroid anodes with robust, spore-forming *Bacillus subtilis* into fully encapsulated, microscale biobatteries. Our innovative approach synergistically combines structural and electrical advantages of 3D-printed stainless steel scaffolds with unmatched biological resilience offered by bacterial endospores. Upon activation, these biobatteries achieve an absolute power output of nearly 1 mW through a series-connected stack of six units, significantly surpassing traditional carbon-based counterparts and demonstrating excellent stability across multiple discharge and recharge cycles. A practical demonstration effectively powers a 3.2 inch thin-film transistor liquid crystal display (LCD) using integrated capacitor-based energy storage. Our work aligns with the emerging trend of additively manufactured electronics (AME), demonstrating the feasibility of cofabricating structural, electrical, and biological components into single, integrated microscale systems.[1] This integration dramatically reduces parasitic effects, simplifies device packaging, and enhances overall sustainability. By bridging critical gaps in microbial bioelectrochemical integration and demonstrating practical viability, our innovative biobattery platform offers a transformative advancement for sustainable, scalable, and biologically resilient energy solutions, significantly accelerating the realization of next-generation autonomous IoT electronics.

2. Results and Discussion

Stainless steel has emerged as a promising anode material for microscale MFCs, owing to its excellent electrical conductivity, mechanical strength, corrosion resistance, and commercial availability.[32] However, its application in miniaturized platforms has been significantly constrained by three critical limitations: 1) incompatibility with conventional microfabrication methods; 2) a characteristically smooth surface that impedes microbial adhesion and biofilm development; and 3) the formation of a passivating oxide layer that limits direct electron transfer between microbial biofilms and the electrode surface.[41,42] To address these challenges, we employ LPBF to fabricate high-resolution stainless steel microarchitectures with precisely tunable porosity, surface roughness, and mechanical integrity. This advanced additive manufacturing technique overcomes the key limitations of traditional stainless steel anodes by enabling seamless microscale integration, improving microbial attachment through increased surface area and texture, and allowing structural designs that promote ionic and electronic transport. Notably, the passivating oxide layer, long considered detrimental to electron transfer, can act as an initial electron sink for electroactive bacteria. Localized microbial metabolism gradually disrupts the oxide, facilitating direct electrical contact with the underlying metal and enhancing charge transfer efficiency. Once the external circuit is closed and electrons are harvested from the biofilm, further corrosion is minimized, preserving long-term electrode integrity. Although a few preliminary studies have investigated 3D-printed stainless steel anodes, particularly gyroid structures, they were largely limited to electrochemical benchmarking and did not evaluate integration into complete MFC systems or demonstrate practical power delivery for real world applications.[43,44] More importantly, none have addressed the long-standing biological challenge of integrating living microorganisms with microscale stainless steel structures for robust, manufacturable power sources. To fill this critical gap, we introduce a novel biocatalytic strategy that combines the structural and electrochemical advantages of 3D-printed stainless steel anodes with the biological durability of bacterial endospores. We demonstrate that *Bacillus subtilis* spores, which are highly resistant dormant forms

of bacteria, can be successfully embedded into stainless steel gyroid scaffolds fabricated by LPBF. This approach uniquely addresses challenges in microbial storage, process compatibility, and long-term viability. Spores can survive harsh environmental conditions, including heat, desiccation, and oxidative stress during fabrication and storage, and can be reactivated via nutrient-triggered germination to resume metabolic activity and power generation. We evaluate the suitability of LPBF-fabricated stainless steel as an anode material by examining its microstructure, biofilm-forming capability, and electrochemical performance. Corrosion behavior and enhancements in electron transfer efficiency are indirectly assessed by comparing our results with established literature. Moreover, we demonstrate the first-ever integration of dormant bacterial spores into these 3D-printed metallic scaffolds, enabling a new class of MFCs that are shelf-stable, robust, and ready for direct integration into microelectronic systems. This dual innovation represents a transformative step toward reliable, manufacturable, and biologically compatible energy solutions for the future of autonomous, distributed electronics.

2.1. 3D Printing of Stainless Steel as a Viable Anode Material

Here, we fabricated stainless steel microbial anodes using LPBF to achieve full powder consolidation and dense, high-resolution microstructures (**Figure 1**). An infrared fiber laser with a maximum power of 200 W was employed to fabricate 3D microporous scaffolds from 316L stainless steel powder (Figure 1a). A high-power infrared fiber laser was employed to construct 3D microporous scaffolds from 316L stainless steel powder (Figure 1a). The resulting structures encompassed a range of geometries and scales (Figure 1b), demonstrating excellent scalability and design flexibility in both porosity and effective volume. The scaffolds were based on a sheet-type triply periodic minimal surface (TPMS), namely the Gyroid, which offers an ideal balance of high surface area, mechanical integrity, and favorable electrochemical characteristics for MFC anodes (Figure S1a, Supporting Information).[43] The LPBF fabrication process involved spreading a uniform layer of stainless steel powder over the build platform, followed by selective laser melting of predefined regions (Figure S1b, Supporting Information). After each scan, the platform was lowered by a fixed layer thickness, and a new powder layer was deposited. This layer-by-layer sequence was repeated until the complete 3D architecture was formed (Figure S1c, Supporting Information). The Gyroid geometry was defined by the following level-set function

$$\sin(X)\cos(Y) + \sin(Y)\cos(Z) + \sin(Z)\cos(X) = c \quad (1)$$

where $X = 2\pi x/3$, $Y = 2\pi y/3$, and $Z = 2\pi z/3$. By tuning the iso-value c, we precisely controlled the scaffold's porosity and morphology, enabling the design of application-specific architectures. Fabrication was carried out using an LPBF system with a laser power of 180 W, scanning speed of 400 mm s^{-1}, layer thickness of 30 µm, hatch spacing of 100 µm, and an inert Argon atmosphere. Four cubic scaffolds with varying dimensions, pore sizes, and equivalent volumes were designed to evaluate structural effects on biofilm growth and electrochemical performance (Figure 1b). Considering the typical size of bacterial cells (≈2 µm) and the average biofilm thickness (≈100 µm), prior studies have shown that micro- and nanoscale pores are highly

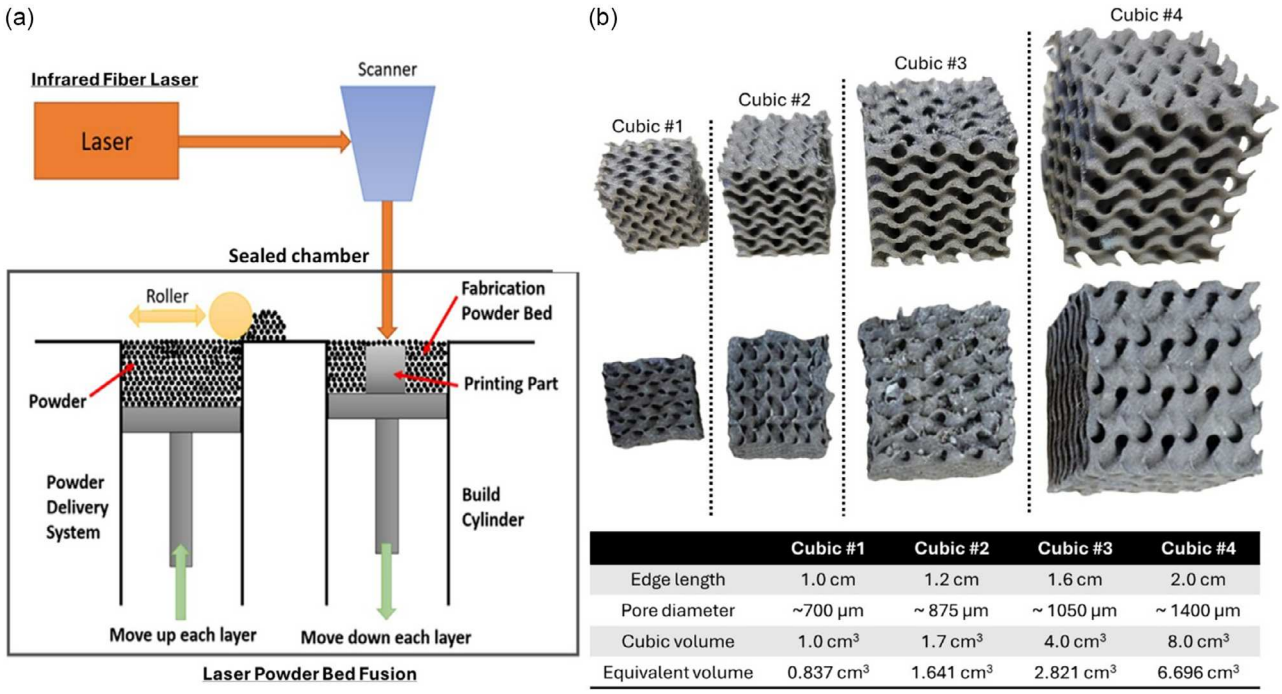

	Cubic #1	Cubic #2	Cubic #3	Cubic #4
Edge length	1.0 cm	1.2 cm	1.6 cm	2.0 cm
Pore diameter	~700 µm	~ 875 µm	~ 1050 µm	~ 1400 µm
Cubic volume	1.0 cm^3	1.7 cm^3	4.0 cm^3	8.0 cm^3
Equivalent volume	0.837 cm^3	1.641 cm^3	2.821 cm^3	6.696 cm^3

Figure 1. 3D Printing of Stainless Steel Electrodes. a) Conceptual illustration of the 3D printing process for fabricating stainless steel electrodes. b) Photographs of 3D-printed stainless steel structures in various sizes and from different angles, accompanied by a table detailing their dimensions and volumes.

susceptible to clogging due to rapid microbial proliferation.[45] This occlusion impedes nutrient diffusion and waste removal, ultimately rendering internal surfaces unsuitable for sustained colonization. To address this, all four designs incorporated submillimeter-porous architectures with large, accessible surface areas to promote efficient mass transport and support the formation of stable, well-distributed internal biofilms. **Figure 2**a shows a high-resolution scanning electron microscope (SEM) image

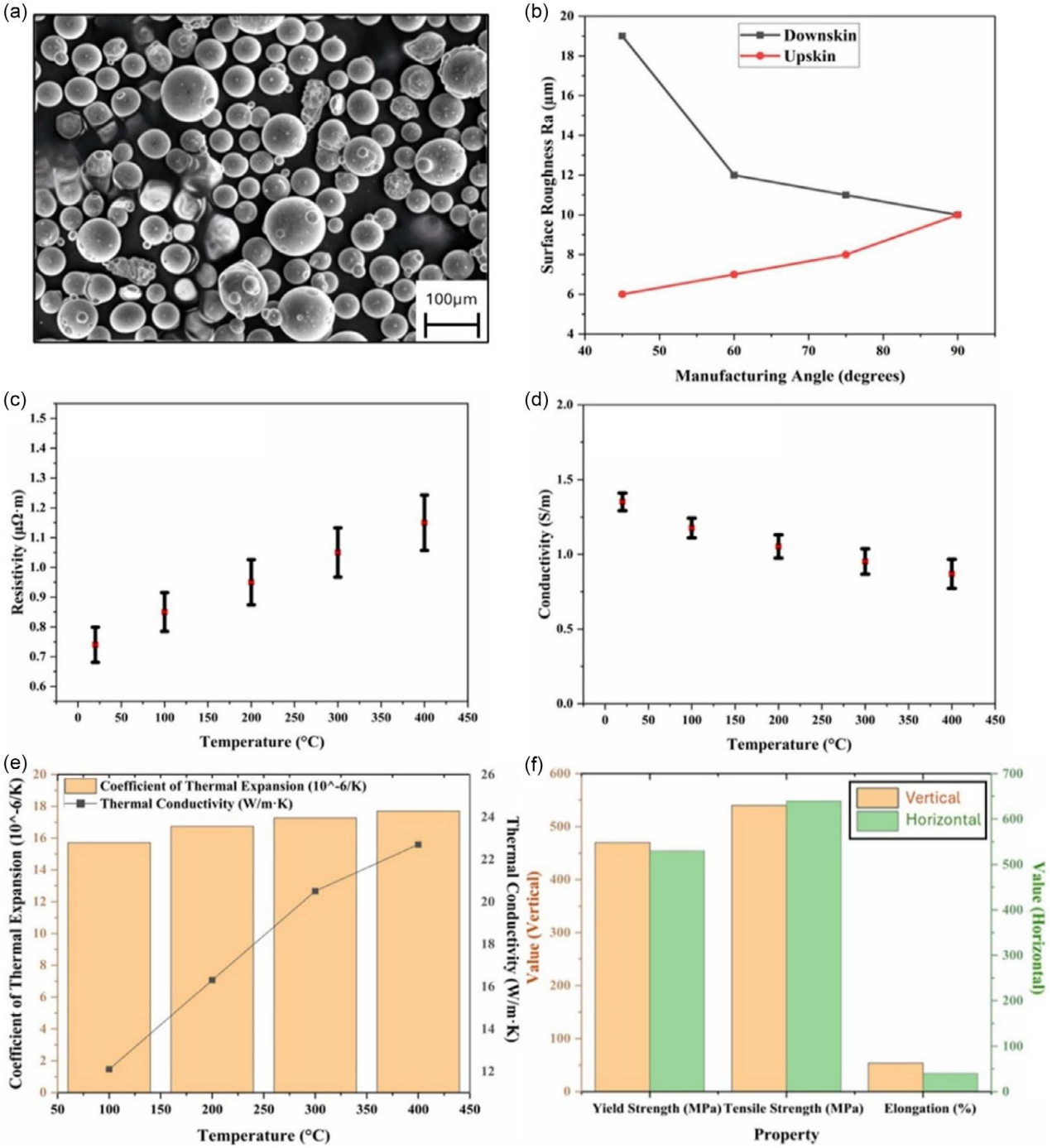

Figure 2. Properties of 3D-printed 316L stainless steel electrodes. a) High-resolution SEM image showing the morphology and particle size distribution of the 316L stainless steel powder. b) Surface roughness of 3D-printed stainless steel electrodes as a function of manufacturing angle. Downskin refers to the bottom-facing surface during printing, often requiring support structures to prevent deformation; Upskin refers to the top-facing surface not in contact with supports. c) Electrical resistivity and d) electrical conductivity of 3D-printed stainless steel electrodes as functions of operating temperature. e) Coefficient of thermal expansion and thermal conductivity of the electrodes across a range of temperatures. f) Mechanical properties, including yield strength, tensile strength, and elongation, of the 3D-printed stainless steel.

demonstrating the morphology, particle sizes, and their size distribution of stainless steel powder used in the 3D printing. The particles appear mostly spherical with a range of sizes, which is indicative of good flowability and packing density. This morphology is crucial for achieving uniform layer deposition during the 3D printing process, ensuring consistent quality and structural integrity of the printed components.[33,34] The spherical shape of the particles minimizes interparticle friction, allowing for smooth and precise layer-by-layer construction. This characteristic is essential for producing high-quality 3D-printed parts with minimal defects, which is critical for applications requiring high mechanical strength and reliability. The morphology and size distribution of stainless steel powder also play a critical role in determining the surface roughness of 3D-printed parts.[33,34,43,44] This is because surface topography in LPBF is directly influenced by how uniformly and densely powder layers are deposited and how completely the particles melt and consolidate. The data clearly demonstrate the precise tunability of surface roughness achievable by simply adjusting the manufacturing angle (Figure 2b). Surface roughness values for 3D-printed 316L stainless steel electrodes range from as low as ≈6 μm to nearly 19 μm, depending on both surface orientation (upskin vs. downskin) and build angle. This broad range indicates that the LPBF process offers a high degree of geometrical and surface control, which is especially advantageous for tailoring surface properties to application-specific requirements. Such control is critical in electro-bio interfaces, where surface topography strongly influences bacterial attachment, electron transfer efficiency, and biofilm development.[32,46,47] For instance, smoother upskin surfaces produced at lower angles can minimize unintended microbial fouling or offer more uniform electrochemical activity, while rougher downskin textures may be purposefully used to enhance microbial adhesion in bioanodes where biofilm formation is desired. Importantly, the ability to converge surface roughness across orientations at 90° further demonstrates the consistency and reproducibility of the LPBF method for microscale feature fabrication. These findings highlight the LPBF process not only as a means for structural fabrication but also as a powerful tool for surface engineering, offering predictable and programmable roughness profiles essential for optimizing performance in bioelectronic and bioenergy systems. 3D-printed 316L stainless steel demonstrates stable and reliable electrical properties across a broad temperature range, making it a strong candidate for MFC anode applications. As shown in Figure 2c, the electrical resistivity increases gradually from ≈0.7 μΩ·m at room temperature to ≈1.3 μΩ m at 400 °C. This modest increase (≈85%) is significantly smaller than that observed in conventional high-conductivity metals like copper, whose resistivity can rise by over 2000% across similar temperature ranges.[48] In parallel, Figure 2d shows that electrical conductivity decreases with increasing temperature, from ≈1.6 to 1.0 S m^{-1}, exhibiting the expected behavior due to increased electron scattering at elevated temperatures. Despite this inverse trend, the overall decline in conductivity is relatively moderate, indicating that stainless steel retains sufficient electron transport capacity under thermal stress. This thermal-electrical stability is further supported by the material's passivation behavior. The chromium-rich oxide layer that naturally forms on stainless steel surfaces is extremely thin (on the nanometer scale) and does not significantly impede bulk conductivity.[49] While it may slightly increase surface resistance, its impact is minimal in systems where bulk charge transfer and interface stability are more critical, such as in MFC anodes. Additionally, this oxide layer enhances corrosion resistance in both aerobic and anaerobic environments,[27,32] offering long-term durability in biologically active, chemically complex MFC settings. Figure 2e presents the temperature-dependent coefficient of thermal expansion (CTE) and thermal conductivity of 3D-printed stainless steel, which are critical parameters for evaluating its suitability as an MFC anode material. The increasing trend in CTE with temperature reflects the material's thermal expansion behavior, which is typical for metals. However, the relatively low and stable CTE (ranging from ≈15 to 18 × 10^{-6} K^{-1}) suggests that 316L can maintain dimensional integrity across a wide thermal range. This is especially important in MFC systems exposed to fluctuating environmental temperatures or internal heat generation from microbial metabolism and electrochemical reactions. Dimensional stability minimizes the risk of mechanical fatigue, delamination, or electrode-biofilm detachment during long-term operation. In parallel, the rising thermal conductivity (from ≈12 to ≈23 W m^{-1} K^{-1} across 100–400 °C) enhances the anode's ability to dissipate heat efficiently. This property helps prevent localized overheating, which could negatively affect microbial viability and electrochemical performance.[50] Enhanced thermal management is also beneficial for maintaining uniform temperature distribution, which supports consistent microbial activity and biofilm growth. Together, these thermal properties, including low thermal expansion and moderate thermal conductivity, highlight the robustness of 316L stainless steel as a 3D printable anode material that can withstand thermal cycling and support stable long-term MFC performance without compromising mechanical or biological integrity. Figure 2f presents the mechanical properties of 3D-printed stainless steel 316L, including yield strength, tensile strength, and elongation, evaluated for samples printed in both vertical and horizontal orientations. The results indicate that the printed structures exhibit high mechanical strength, with both yield and tensile strengths approaching or matching those of conventionally manufactured stainless steel. This suggests that the additive manufacturing process retains the inherent strength of the material, even in complex architectures like porous lattices. Notably, while the tensile strength is slightly higher in the horizontal orientation, the vertical build direction shows marginally greater elongation, reflecting enhanced ductility. Elongation (%), which quantifies the material's capacity for plastic deformation before failure, is especially critical for pore-skeleton structures, where flexibility helps prevent crack propagation and mechanical failure under stress or vibration. These findings underscore the robustness and mechanical reliability of the 3D-printed stainless steel structures. For microscale bioelectronic or energy devices, such as MFC anodes, these mechanical characteristics are crucial for ensuring long-term integrity under operational loads, thermal expansion, and potential biofilm-induced stress.

2.2. Endospores as Dormant and Resilient Biocatalysts for 3D-Printed Stainless Steel Anodes

The use of living microorganisms as biocatalysts in MFCs presents significant challenges for integration into practical,

miniaturized electronic systems. Issues such as compatibility with microfabrication, maintenance of microbial viability during storage and operation, and long-term stability have limited MFCs to proof-of-concept demonstrations. To address these constraints, our group previously explored freeze-dried microorganisms as a route to enhance storage and facilitate device assembly.[51] While freeze-drying preserved metabolic viability to some extent, the resulting cells were extremely sensitive to handling, and their rehydration required tightly controlled conditions. Moreover, freeze-dried cultures proved difficult to integrate into fabrication workflows, limiting their utility for scalable, manufacturable systems. Building on this work, we also demonstrated the viability of *Bacillus subtilis* as a spore-forming electrogenic bacterium in sweat-activated wearable MFCs.[38–40] In those systems, *B. subtilis* exhibited repeated cycles of germination and sporulation in response to the presence or absence of sweat, enabling long-term intermittent energy generation in bioelectronic applications.

In this study, we present a significant advancement: the first integration of *B. subtilis* endospores with 3D-printed stainless steel anodes fabricated via LPBF. This innovation addresses the long-standing limitations of biological instability and microfabrication incompatibility by uniting a highly durable biocatalyst with a structurally and electrically optimized anode platform. Spores, unlike vegetative cells or freeze-dried counterparts, tolerate extreme conditions including heat, desiccation, and chemical stress, making them uniquely suitable for incorporation into advanced manufacturing processes.[37] To prepare the spore-integrated bioanode, vegetative *B. subtilis cells* were seeded onto LPBF-fabricated stainless steel gyroid scaffolds, where they adhered, acclimated, and formed a dense biofilm. Following nutrient deprivation, sporulation was induced, resulting in a robust round-shape spore-based biofilm that could be stored or processed without degradation (Figure S2a, Supporting Information). Upon rehydration with a defined germinant solution (AGFK: L-asparagine, D-glucose, D-fructose, and potassium ions), the dormant spores reactivated into metabolically active, rod-shaped cells (Figure S2b, Supporting Information), gradually increasing power output as metabolic activity resumed. This approach redefines the role of biocatalysts in MFCs, shifting them from fragile biological components requiring careful preservation to stable, integratable elements that can be stored and deployed like conventional materials. By combining the mechanical, thermal, and electrical advantages of 3D-printed stainless steel with the biological durability of bacterial endospores, this work provides a transformative solution for enabling shelf-stable, microfabrication-compatible, and reactivatable biobatteries.

2.3. Biofilm, Corrosion, and Electrochemical Roles of 3D-Printed Stainless Steel Electrodes

Conventional stainless steel mesh, long used as an anode in macroscale MFCs,[30] presents fundamental limitations for miniaturized platforms. Its smooth surface texture impedes microbial adhesion and fails to support dense, electroactive biofilm formation, which is critical for efficient electron transfer in bioelectrochemical systems.[41,42] Our work introduces a transformative solution through 3D-printed stainless steel electrodes, which address these shortcomings with finely tunable surface roughness, tailored porosity, and architecturally optimized frameworks. As detailed in Section 2.1, these design freedoms can substantially enhance bacterial colonization and facilitate efficient nutrient and waste exchange, paving the way for high-performance micro-MFCs with robust long-term operation. The printed architecture not only maximizes the effective surface area but also introduces macroporous pathways that prevent pore clogging, which is a major issue in microbial systems. This architectural control, enabled by LPBF, offers a unique opportunity to rationally engineer the physical and electrochemical interface between the electrode and biology, overcoming the traditional tradeoff among mechanical strength, microbial accessibility, and electrical conductivity. A notable feature of stainless steel is its passivation oxide layer, often regarded as an obstacle to electron transfer. However, our findings suggest a paradigm shift: The ultrathin oxide layer provides a biocompatible, bioaffinitive surface that promotes early-stage microbial adhesion. Following 24 h of vegetative growth and induced sporulation, SEM imaging reveals a uniform distribution of resilient, round-shaped spores attached to the porous scaffold (**Figure 3**a). Energy-dispersive X-ray spectroscopy (EDS) confirms the accumulation of essential biofilm components (C, N, and O), and longer cultivation (48 h) further intensifies biofilm density, with increased C and N signals and the emergence of a phosphorus peak, which indicates the presence of polysaccharides, nucleic acids, and phospholipids essential for extracellular matrix stability (Figure 3b). Concurrently, the progressive decline in Fe and Cl peaks suggests increasing coverage of the stainless steel surface by the developing biofilm, which physically masks the underlying substrate. More notably, the unexpected decrease in the O peak, despite the accumulation of organic material, suggests that the native oxide layer is being altered or reduced by biofilm activity. Given that oxygen is a major component of both the passive oxide layer and organic biofilm constituents, a reduction in the O signal is counterintuitive if biofilm thickness alone were increasing. This observation implies that the microbial activity is not simply coating the surface but actively modifying it, likely through localized microbially induced corrosion or enzymatic reduction of the oxide layer. Although EDS lacks the surface sensitivity and depth resolution required to precisely detect nanometer-thick passive films, the observed trends align with previous findings that electrogenic bacteria can interact with and disrupt metal oxide layers to enhance extracellular electron transfer.[49] The thinning or partial removal of the oxide layer could expose more conductive stainless steel beneath or alter surface chemistry in ways that facilitate electron tunneling or direct contact-based transfer. Thus, the decline in the O peak serves as indirect but compelling evidence of bioelectrochemical interface evolution, reinforcing the idea that the 3D-printed stainless steel surface becomes more electrochemically favorable over time through bacterial activity. These surface transformations likely decrease interfacial resistance and improve direct electron transfer (DET) or mediated electron transfer (MET), especially via secreted flavins in *Bacillus subtilis*.[52] Electrochemical measurements substantiate these findings. Cyclic voltammetry (CV) profiles reveal a dramatic enhancement in redox activity from the bare electrode to day 0 post-inoculation, with diminishing returns by day 1 and stabilization by day 10 (Figure 3c).

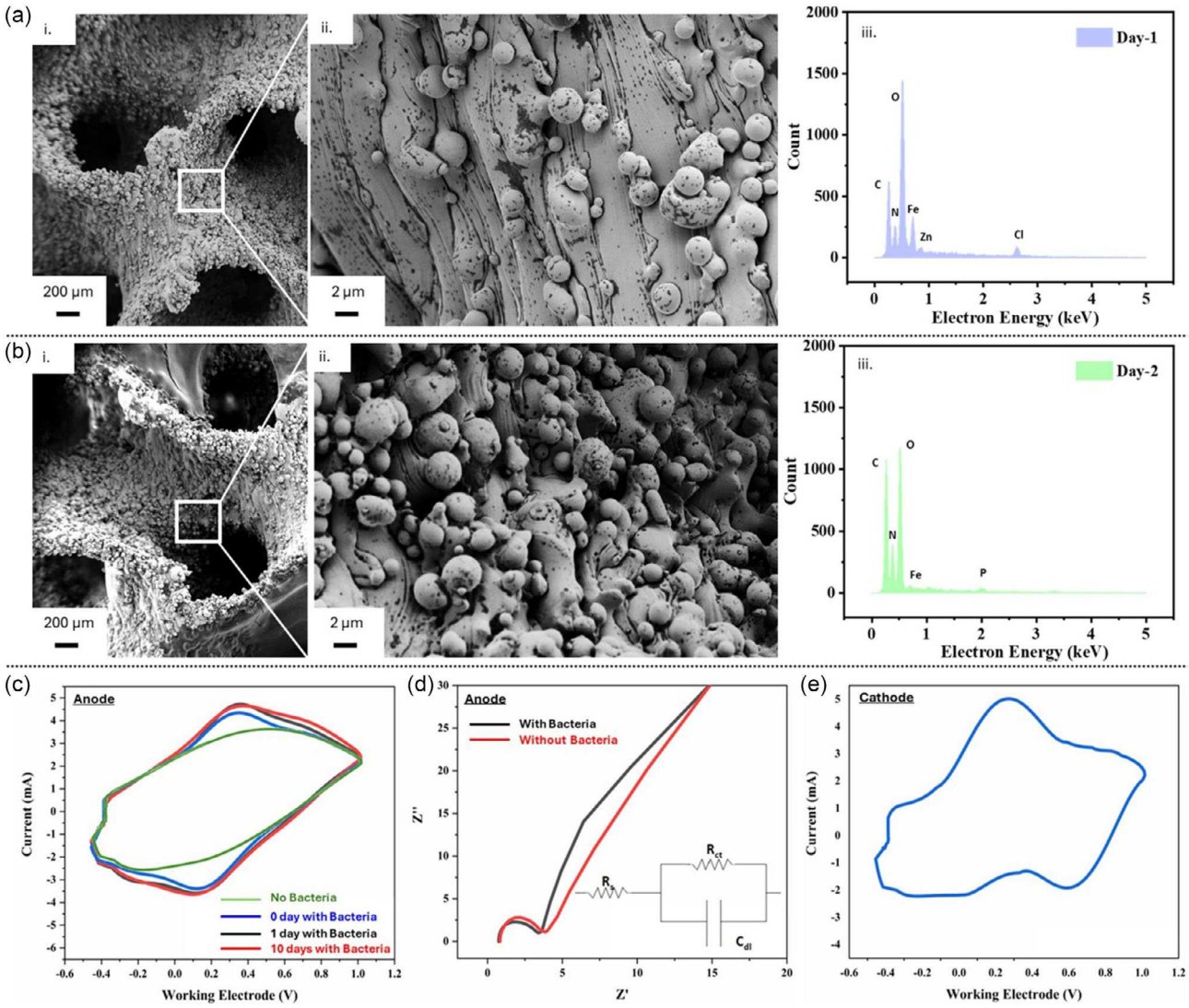

Figure 3. Electrochemical performance of 3D-printed 316L stainless steel electrodes. SEM images and magnified views showing *Bacillus subtilis* biofilm formation on 3D-printed stainless steel surfaces at a) Day 1 and b) Day 2, along with corresponding EDS analyses. c) CV profiles of stainless steel anodes over 0, 1, and 10 days of biofilm growth, compared to a sterile control. d) EIS of stainless steel electrodes with and without bacterial biofilm, including the fitted equivalent circuit model. e) CV profile of a stainless steel electrode coated with Pt/C catalyst, functioning as an air-breathing cathode.

This rapid establishment of a metabolically active, electroactive biofilm underscores the suitability of our electrodes for time-sensitive and low-maintenance applications. Electrochemical impedance spectroscopy (EIS) complements this insight, with the biofilm-covered electrode exhibiting a smaller semicircle in the Nyquist plot, indicating reduced charge transfer resistance (Rct) and more efficient electron kinetics (Figure 3d). Beyond anode performance, our platform exhibits multifunctionality and integration potential. By simply applying a Pt/C catalyst layer, a 3D-printed scaffold serves as a high-performance air-breathing cathode (Figure 3e). The cathode demonstrates sharp, well-defined redox peaks and low overpotentials, further showcasing the structural and electrochemical adaptability of our design. This work represents a significant advancement in bioelectrochemical interface engineering. Unlike conventional carbon-based materials or planar electrodes,[9,20,21] our stainless steel platform merges precision manufacturing, microbial compatibility, and electrochemical efficiency, providing a scalable and cost-effective solution for powering next-generation microdevices. The ability to leverage spore-forming microbes adds a powerful dimension of long-term storage and on-demand activation, making our system ideal for transient, wearable, and ingestible electronics that require self-sustaining energy sources with minimal maintenance. Furthermore, this study opens new research directions in microbially induced surface engineering and the co-design of electrode materials and microbial systems. Our findings challenge conventional views on oxide layers as barriers and instead position them as dynamic interfaces that can evolve to enhance bioelectronic function.

2.4. Biobattery Design, Operation, and Performance

The use of 3D printing to fabricate metallic, porous, and mechanically robust anodes offers transformative potential for the design, integration, and performance of MFCs, ultimately facilitating their transition to practical real-world applications. Traditionally, both macro- and microscale MFCs have relied on modular fabrication, in which the anode, cathode, and PEM are fabricated separately and manually assembled. While this approach offers flexibility and is well-suited for prototyping, it introduces significant limitations to performance and scalability. Manual alignment and sealing increase the risk of misalignment, leakage, and mechanical failure, particularly in compact or fluidic environments. Electrical and mechanical interconnects between discrete modules can lead to parasitic effects such as contact resistance and signal loss, undermining system efficiency. Moreover, the need for connectors and structural interfaces enlarges the device footprint and hinders miniaturization. Material incompatibilities between components further complicate bonding, and long-term environmental exposure can degrade mechanical integrity. While modular fabrication may be viable at small scales, it becomes less practical for mass production due to increased labor demands, assembly complexity, and quality control burdens. Ideally, monolithic fabrication integrates all components through a single, unified process, eliminating many of these issues.[53] However, this approach is not currently feasible for MFCs. Each component, especially the PEM, requires distinct materials and processing conditions that are incompatible with monolithic integration.[16] For example, common PEM materials such as Nafion cannot be easily microfabricated or co-processed with metallic structures. Recognizing these challenges, we developed a refined modular fabrication strategy that minimizes the traditional drawbacks of modular assembly while maintaining scalability and performance (**Figure 4**a). In our system, the anode, cathode, and sealing cover were all 3D printed using stainless steel (Figure 4b and S3a,b, Supporting Information), allowing for precise dimensional control, excellent mechanical compatibility, and material uniformity (Figure 4c,d and S3c,d, Supporting Information). This uniformity facilitates straightforward assembly with minimal alignment errors. The cathode was further engineered into an air-breathing electrode by applying an electroless Pt/C catalyst coating, while the inner surface was brushed with a Nafion solution to form a thin, solid proton-conductive film that functions as a PEM (Figure 4b). Nafion, a sulfonated tetrafluoroethylene-based fluoropolymer-copolymer, is widely used in MFCs and proton exchange systems due to its high ionic conductivity and chemical stability. In solution form, it can be applied to surfaces and dried into a continuous membrane layer, which is especially advantageous in miniaturized or irregular geometries where conventional PEM sheets are unsuitable. This design enabled a compact, tightly sealed sandwich configuration of anode–membrane–cathode (Figure S3c,d, Supporting Information), assembled with high reproducibility and minimal variation in performance across devices (Figure 4e). Platinum wires were directly soldered to the stainless steel anode and cathode prior to the Pt/C catalyst coating, using an organic flux specifically chosen to avoid redox reactions in aqueous environments. This ensured a stable and low-resistance electrical connection. After soldering, the wire junctions were encapsulated in a water-resistant epoxy resin to provide electrical insulation and protect the connections from environmental exposure. The insulated wires were carefully routed through predrilled holes in the sealing cover, preventing mechanical stress and minimizing the risk of short-circuiting during operation. Despite the use of a modular assembly approach, our fabrication strategy resulted in robust, reproducible, and reusable MFC units. As shown in Figure 4f, power output remained stable across multiple cycles of use and cleaning, demonstrating the durability of the stainless steel components and the mechanical integrity of the overall system. These results highlight the effectiveness of our advanced modular design, which uses precise 3D printing and strategic material choices as a practical and scalable alternative to monolithic fabrication for next-generation bioelectronic devices. Additionally, Figure 4g illustrates a clear linear increase in power output with increasing anode size (referencing Cubic structures from Figure 1b), validating the system's scalability and predictable performance trends.

Bacillus subtilis vegetative cells were first used to form a biofilm on the stainless steel anode, followed by induced sporulation directly on the electrode surface. Upon introduction of the AGFK germinant, the MFC achieved full germination and stable power generation within ≈25 min (black squares) (Figure 4h). In contrast, when spores were introduced directly onto the anode without prior biofilm formation, their attachment was weaker, resulting in a delayed onset of stable power output (red circles). However, as previously reported,[28] pretreating the spores with sublethal heat at 70 °C increased their germination probability. This thermal activation significantly shortened the germination time, enabling stable power generation within 20 min of AGFK introduction (blue triangles). Figure 4i presents the voltage and power output of the MFC as a function of current across a range of external resistors (open circuit, 470, 250, 162, 100, 71, 47.5, 32, 22, 15, 10, 2, 1.5, 0.45, and 0.35 kΩ). The maximum absolute power output of 130 μW (equivalent to 155 μW cm^{-3}) was achieved with a 32 kΩ load, which closely matched the internal resistance of the system.[14,15] This power was generated solely by microbial metabolic activity, as the abiotic control produced only 3 μW (Figure S4a, Supporting Information), confirming the biological origin of the electricity. Although *Bacillus subtilis*, a Gram-positive species, is typically considered weakly electrogenic due to its thick and potentially insulating cell wall,[29] the power output of this spore-forming organism was comparable to that of stronger non-spore-forming exoelectrogens, such as *Shewanella oneidensis* MR-1 (Figure S4b, Supporting Information) and *Synechocystis* sp. PCC6803 (Figure S4c, Supporting Information). When the MFC was connected to a 100 kΩ resistor, which was much higher than the internal resistance, it exhibited stable current output over time (Figure 4j), indicating sustainable electron production. In contrast, under a 1 kΩ load, where the external resistance was significantly lower than the internal resistance, current generation declined over time. This drop suggests that the electron extraction rate exceeded the metabolic electron generation capability of the bacteria, leading to performance decay. While many 3D-printed MFCs using various anodic materials such as paper, polymers, or carbon materials report high power densities, their absolute

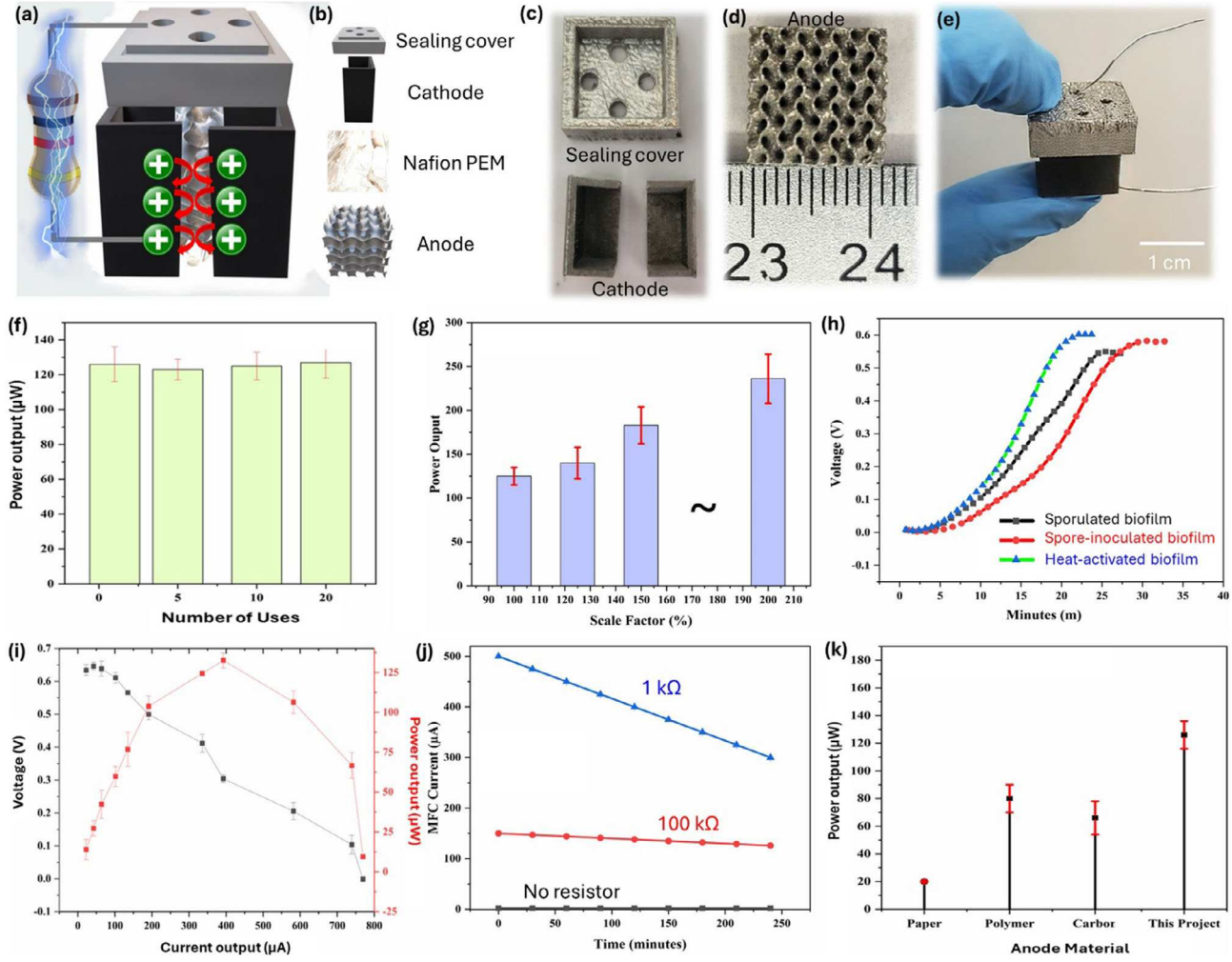

Figure 4. Design, fabrication, and performance of the microbial biobattery. a) Conceptual illustration of the assembled microbial biobattery. b) Exploded view showing individual components. c) Photographs of the 3D-printed stainless steel cathode and sealing cover. d) Image of the 3D-printed anode with dimensions shown using a ruler for scale. e) Assembled microbial biobattery device. f) Power output stability over multiple reuse cycles, demonstrating durability. g) Power output as a function of anode size, showing scalability (100%, Cubic #1; 125%, Cubic #2; 150%, Cubic #3; and 200%, Cubic #4; as defined in Figure 1b). h) Voltage profiles of MFCs formed using different spore-based biofilm strategies, highlighting differences in germination time. i) Voltage and power output as a function of current across a range of external resistors. j) Time-dependent current output under different external load resistances. k) Comparison of absolute power output from 3D-printed MFCs using various anodic materials.[54–58]

power output often remains insufficient for real-world applications (Figure 4k).[54–58] In contrast, our miniature stainless steel-based biobattery demonstrated both high power density and high absolute power, offering a practical and scalable solution for powering low-power electronics and autonomous sensors.

2.5. Biobattery Stack for Chip-On-Board Power Generation

To deliver sufficient electrical output for practical applications, low-power microbial biobatteries must be connected in parallel or series. However, in conventional systems, nonstandardized and unreliable modular assembly often results in substantial performance variability across individual cells. This imbalance can severely degrade overall output rather than improving it, ultimately rendering microbial biobatteries impractical as power sources for electronic devices. In parallel configurations, performance mismatches can induce circulating currents, where stronger cells drive current into weaker ones, leading to energy loss, internal heating, and long-term degradation.[59] In series configurations, a more critical issue known as voltage reversal may occur when underperforming cells are forced into reverse bias.[60] This phenomenon can irreversibly damage the affected cell by disrupting the electrogenic biofilm and shifting the microbial population toward less electroactive species. These challenges become even more severe at the microscale, where fabrication artifacts from manual assembly such as misaligned electrodes, inconsistent sealing, variable membrane thickness, and uneven biofilm development can significantly impair the performance of individual cells.[61] Additionally, limited fuel accessibility and poor mass transport in tightly packed or

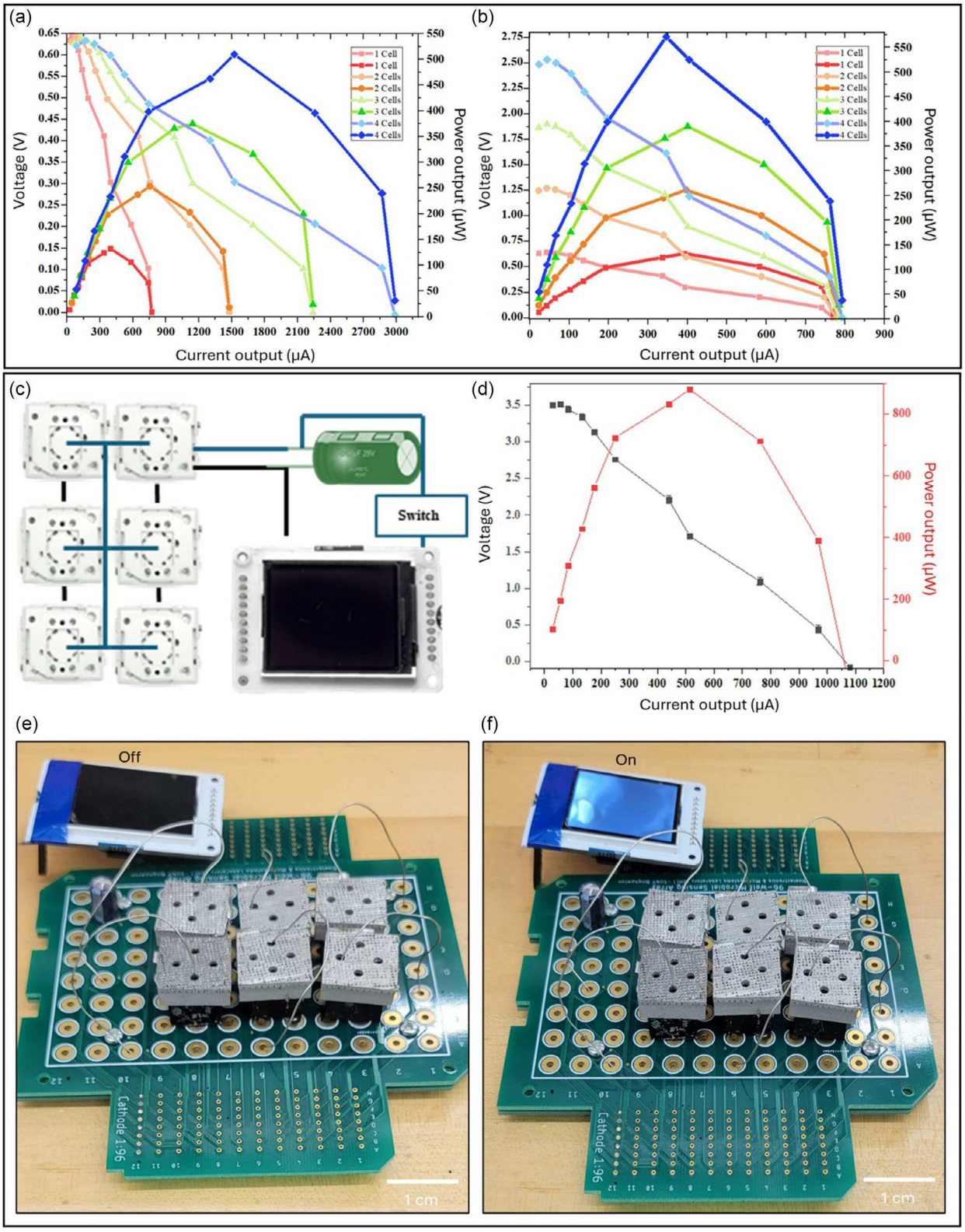

Figure 5. Biobattery stack for chip-on-board power generation. a) Voltage and power output of a biobattery stack consisting of four units connected in parallel. b) Voltage and power output of a biobattery stack with four units connected in series. c) Voltage and power output of the six-unit series-connected biobattery stack. d) Schematic diagram of an LCD operating system powered by a stack of six serially connected biobatteries via a capacitor. e) Photograph of the LCD system in the OFF state prior to capacitor discharge. f) Photograph of the LCD system in the ON state following capacitor discharge.

low-porosity designs contribute to further performance mismatches and instability.

In contrast, our 3D-printed stainless steel MFCs offer a breakthrough solution to these limitations. Through additive manufacturing, we can precisely fabricate mechanically robust and electrochemically reliable MFC units with highly consistent performance. The stainless steel electrodes featured a submillimeter-porous architecture, carefully designed to avoid pore clogging while enabling effective nutrient diffusion and waste removal (Figure S2, Supporting Information). This promoted uniform microbial colonization and sustained biofilm activity. As a result, both parallel and series stacking of the biobatteries were achieved without any signs of circulating currents or voltage reversal. In parallel configurations, total current output scaled linearly with the number of connected units (**Figure 5**a). Likewise, in series configurations, voltage output increased proportionally, demonstrating predictable, stable, and robust system performance (Figure 5b). These results confirm that our 3D-printed stainless steel MFCs provide a scalable and practical biopower platform capable of supporting the energy demands of next-generation electronics.

To demonstrate the practical potential of our biobattery stack, we powered a relatively high-demand electronic device: a 3.2 inch thin-film transistor liquid crystal display (TFT-LCD) panel, which requires an operating voltage of ≈3.0 V and a current of 10 mA. To meet this voltage requirement, six biobatteries were connected in series, delivering an open-circuit voltage of 3.5 V, a maximum current of 1 mA, and a peak power output of 900 μW (Figure 5c). Given the mismatch between the continuous output of the MFCs and the pulsed power demand of the LCD, a 22 mF electrolytic capacitor was integrated for power conditioning and delivery (Figure 5d). This energy storage element allowed the biobattery stack to accumulate charge over time and deliver it in a short burst sufficient to activate the LCD. The transition from the OFF state (Figure 5e) to the ON state (Figure 5f) after capacitor discharge confirms that our system can efficiently store and release energy on demand. Importantly, the entire power system, which includes the stacked biobatteries, capacitor, and control circuitry, was integrated into a chip-on-board configuration to enable compact and self-contained energy delivery directly at the point of use. This demonstration highlights the scalability, reliability, and real-world applicability of our 3D-printed stainless steel MFCs. Their ability to support series and parallel configurations without performance degradation, combined with seamless integration into chip-scale electronics, positions this platform as a promising energy solution for distributed, autonomous, and intermittently powered microelectronic systems.

3. Future Outlook and Remaining Challenges

The successful integration of spore-forming bacteria with 3D-printed stainless steel MFCs represents a major step toward sustainable, durable, and manufacturable bioenergy systems compatible with future microelectronics. However, several challenges must still be addressed to realize their full potential in ubiquitous applications. From a fabrication perspective, integration with standard microelectronic processes remains a barrier. While LPBF provides unmatched precision for metal-based architectures, future efforts may focus on the co-printing of bio-compatible polymers, sensors, and protective coatings, enabling fully integrated, low-footprint energy platforms. The incorporation of dry-process PEMs or ionomers, beyond cast Nafion coatings, may facilitate monolithic integration of ionic interfaces. On the system level, energy management and adaptive load balancing are critical. As shown in the LCD demonstration, capacitors are effective for buffering intermittent power, but intelligent power management circuits could further optimize energy harvesting and release across irregular demand cycles. Coupling these systems with low-leakage mixed-signal electronics or sleep-mode processors will allow complete self-powered microsystems. Finally, regulatory and biosafety concerns must be addressed for widespread deployment. Although *Bacillus subtilis* is widely regarded as safe (GRAS status), large-scale deployment of bioelectronic devices must comply with microbial containment and disposal standards, particularly for medical or environmental monitoring applications.

4. Conclusion

In this study, we demonstrated a transformative approach to MFC technology by integrating 3D-printed 316L stainless steel gyroid anodes with spore-forming *Bacillus subtilis*, creating the first microscale biobattery platform that is both structurally robust and biologically resilient. Leveraging LPBF, we fabricated highly conductive and architecturally optimized anodes with tunable surface roughness and submillimeter porosity, which are critical features for enhancing microbial adhesion, biofilm development, and efficient electron transfer. The integration of bacterial endospores, which can withstand harsh fabrication, storage, and operational conditions, further enabled long-term viability, shelf stability, and reactivation on demand through nutrient-triggered germination. Our biobattery system achieved an absolute power output of 130 μW, operated reliably through multiple reuse cycles, and was scalable through both series and parallel configurations without performance degradation. Integration into a chip-on-board power system demonstrated its practical potential by intermittently powering a thin-film LCD using a capacitor-assisted energy buffer. Despite using a modular fabrication strategy, the design achieved high reliability and reusability, rivaling monolithic systems in integration quality and performance consistency. These advances collectively address long-standing barriers in MFC miniaturization, including material compatibility, biocatalyst viability, and system integration. The demonstrated platform provides a scalable, durable, and sustainable power solution for real electronics, opening new opportunities in IoT nodes, biomedical implants, smart packaging, and transient electronics.

5. Experimental Section

B. subtilis Inoculation and Induced Sporulation: *Bacillus subtilis* strain 168, obtained from the American Type Culture Collection (ATCC), was initially grown in Luria Broth (LB) at 37 °C with gentle agitation for 24 h. Bacterial growth was tracked by measuring the optical density at 600 nm (OD_{600}), and cultures were harvested once OD_{600} reached ≈1.0, corresponding to ≈10^9 CFU mL^{-1}. The cells were then centrifuged and resuspended in fresh

LB medium for downstream use. To induce sporulation on the stainless steel anodes, the biofilm-forming cultures were subjected to nutrient-limited conditions known to trigger spore formation under environmental stress. These anode-mounted cultures were incubated aerobically at 37 °C, where sporulation typically occurred within 24–48 h. For experiments involving direct spore inoculation, *B. subtilis* cultures were spread on nutrient-depleted agar plates to initiate sporulation. Harvested spores underwent purification steps to eliminate residual vegetative cells and nonviable spores, yielding a highly pure spore preparation for experimental use.

Preparation of Germinant Solution: The germinant solution was prepared by combining LB medium with 10 mM L-Valine and a nutrient mixture referred to as AGFK, consisting of 10 mM L-asparagine, 33.6 mM D-glucose, 33.6 mM D-fructose, and 60 mM potassium chloride (KCl), all sourced from Sigma–Aldrich. Upon exposure to this germinant blend, spherical *B. subtilis* spores underwent morphological transition into elongated, rod-shaped vegetative cells. This germination process is regulated by specific receptors: GerA, which is activated by L-Valine, and GerB and GerK, which are responsive to the AGFK components.[28,29]

Inoculation with Other Bacterial Strains: *Shewanella oneidensis MR-1* was retrieved from a −80 °C glycerol stock and cultured in 20 mL of LB medium at 37 °C with gentle shaking overnight. Following incubation, cells were collected via centrifugation to remove excess biomass and resuspended in fresh LB to an OD_{600} of ≈1.0 for subsequent experiments. *Synechocystis* sp. PCC 6803, obtained from the ATCC, was cultured in 25 mL of BG-11 medium in shake flasks under controlled light conditions. Cultures were maintained at 30 °C in a VWR Signature Diurnal Growth Chamber under a 12 h light/12 h dark photoperiod for two weeks. The BG-11 medium formulation included 6 mg of citric acid, 40 mg of K_2HPO_4, 75 mg of $MgSO_4$, 1.5 g of $NaNO_3$, 36 mg of $CaCl_2$, 1 mg of EDTA, and 6 mg of ferric ammonium citrate per liter of distilled water. Cultures were considered ready for experimentation when they reached an OD600 of ≈1.0.

SEM Imaging: To prepare samples for SEM imaging, bacterial cells were first fixed in a 2% glutaraldehyde solution prepared in 0.1 M phosphate-buffered saline (PBS, pH 7.4) at 4 °C for 8 h to preserve cellular structure. After fixation, samples were gently rinsed with PBS to remove residual fixative. Dehydration was carried out using a freeze-drying method to prevent structural collapse associated with liquid drying. The fully dehydrated samples were then sputter-coated with a thin conductive layer of carbon using a 208HR Turbo Sputter Coater (Cressington Scientific Instruments, UK) to minimize charging under the electron beam. Imaging was performed using a high-resolution field emission scanning electron microscope (FE-SEM; Supra 55 VP, Carl Zeiss AG, Germany) under high vacuum conditions, allowing for detailed visualization of biofilm morphology and surface interactions with the electrode.

3D Printing of Stainless Steel: The 3D anodes were fabricated from 316L stainless steel powder using LPBF, producing dense, high-resolution microstructures with excellent mechanical robustness. Printing was performed in an inert argon environment using a 180 W fiber laser, with a scan speed of 400 mm s^{-1}, a layer thickness of 30 µm, and a hatch spacing of 100 µm.

The electrode architecture employed a TPMS topology, specifically the Gyroid structure, chosen for its continuous curvature and highly interconnected porosity. During fabrication, uniform powder layers were deposited onto the build platform and selectively fused according to CAD-defined geometries. After each layer was completed, the platform was incrementally lowered to enable sequential layering, ultimately generating complex, fully 3D structures. Multiple Gyroid-based cubic variants were printed, varying in external dimensions, pore sizes, and overall volume to systematically evaluate their potential for microbial attachment and electrochemical performance.

Sealing Cover and Cathode Preparation: The sealing covers and cathodes were fabricated using the same LPBF process employed for the anodes, utilizing 316L stainless steel powder and identical printing parameters. The sealing covers were used without additional modification, while the cathodes underwent mechanical polishing to increase surface roughness and improve coating adhesion. To functionalize the cathodes, a Pt/C catalyst layer was applied by immersing the printed structures in a suspension of Pt/C powder dissolved in 30 mL of dimethyl sulfoxide (DMSO). After each immersion, the cathodes were dried at 60 °C for 30 min. This dip-coating and drying process was repeated multiple times to achieve a uniform catalytic layer. Subsequently, a proton exchange interface was established by brushing the inner surface of each cathode with a 25 wt% Nafion dispersion (20 mL total volume). The coated electrodes were then dried at 100 °C for 1 h to ensure complete solvent evaporation and membrane stabilization.

Electrical Connection and Device Assembly: Prior to bacterial inoculation of the anode and Pt/C functionalization of the cathode, platinum wires were soldered to each electrode to enable electrical output collection. An organic flux compatible with aqueous environments and nonreactive under redox conditions was used to ensure stable electrical connections without introducing electrochemical interference. Following soldering, the exposed sections of the platinum wires were coated with a water-resistant epoxy resin to insulate the connections and protect them from environmental exposure. Subsequently, the anodes were inoculated with *B. subtilis* to establish spore-based biofilms, and the cathodes were functionalized with Pt/C and Nafion as described above. Each component, including the anode, PEM, and cathode, was then assembled into a compact sandwich configuration. The use of precisely 3D-printed parts enabled seamless, alignment-free assembly, similar to a modular "Lego-like" system. The platinum wire connected to the anode was routed through a predrilled hole in the sealing cover, ensuring mechanical protection and preventing the risk of short-circuiting during operation.

Electrical Characterization Setup: The electrical output of the biobatteries was characterized using a data acquisition system (DI-4108U, DATAQ Instruments, USA) connected across a series of external resistors. Voltage measurements were recorded under varying resistive loads, including the following resistor values: open circuit (no resistor), 470, 250, 162, 100, 71, 47.5, 32, 22, 15, 10, 2, 1.5, 0.45, and 0.35 kΩ. From the recorded voltage drops across each resistor, the corresponding current and power outputs were calculated.

Electrochemical Characterization Setup: CV and EIS were conducted using a Squidstat Plus potentiostat (Admiral Instruments). All measurements were carried out in a standard three-electrode configuration, with a platinum foil serving as the counter electrode and an Ag/AgCl electrode (saturated KCl) as the reference. For CV analysis, the potential was swept from –0.5 to 1.0 V at a scan rate of 100 mV s^{-1}. EIS measurements were performed at an excitation voltage of 0.5 V over a frequency range spanning from 0.1 Hz to 100 kHz.

Statistical Analysis: Electrical performance measurements were based on a minimum of three independent experiments to ensure consistency and reproducibility. Data are reported as mean values with corresponding standard error (SE), unless specified otherwise. Statistical analysis and data visualization were performed using Origin software (OriginLab, USA) to ensure accurate interpretation and presentation of results.

Supporting Information

Supporting Information is available from the Wiley Online Library or from the author.

Acknowledgements

This work was supported by the National Science Foundation under grant no. 2410431 and by the State University of New York (SUNY) System Administration through the SUNY Research Seed Grant Program (grant no. 241000). The authors gratefully acknowledge the Analytical and Diagnostic Laboratory at SUNY Binghamton for providing access to essential instrumentation and facilities. Language refinement and grammar correction during manuscript preparation were assisted by ChatGPT, with all final content thoroughly reviewed and approved by the authors. The authors take full responsibility for the findings and interpretations presented in this article.

Conflict of Interest

The authors declare no conflict of interest.

Data Availability Statement

The data that support the findings of this study are available from the corresponding author upon reasonable request.

Keywords

additive manufacturing, microbial biobatteries, microbial fuel cells, spore-based biocatalysts, stainless steel

Received: May 15, 2025
Revised: July 3, 2025
Published online:

[1] L. Portilla, K. Loganathan, H. Faber, A. Eid, J. G. D. Hester, M. M. Tentzeris, M. Fattori, E. Cantatore, C. Jiang, A. Nathan, G. Fiori, T. Ibn-Mohammed, T. D. Anthopoulos, V. Pecunia, *Nat. Electron.* **2023**, *6*, 10.
[2] M. A. Jamshed, K. Ali, Q. H. Abbasi, M. A. Imran, M. Ur-Rehman, *IEEE Sens. J.* **2022**, *22*, 5482.
[3] S. Voges, K. F. Becker, D. Schutze, B. Schroder, P. Fruehauf, M. Heimann, S. Nerreter, R. Blank, S. Gottwald, A. Hofmeister, M. Schmied, M. Kreitmair, R. Fust, W. Neifer, T. Braun, T. Thomas, M. Schneider-Ramelow, K. D. Lang, *Int. Symp. Microelectron.* **2019**, *1*, 415.
[4] A. Elhadad, L. Liu, S. Choi, *J. Power Sources* **2022**, *535*, 231487.
[5] S. Choi, *Small* **2022**, *18*, 2107902.
[6] D. R. Lovley, *Annu. Rev. Microbiol.* **2012**, *66*, 391.
[7] C. Zheng, K. Dai, D. Liu, F. Yi, X. Wang, L. Zhu, Z. You, *Adv. Sci.* **2020**, *7*, 2000254.
[8] F. Calignano, T. Tommasi, D. Manfredi, A. Chiolerio, *Sci. Rep.* **2015**, *5*, 17373.
[9] S. Choi, *Biosens. Bioelectron.* **2015**, *69*, 8.
[10] G. G. Kumar, V. G. S. Sarathi, K. S. Hahm, *Biosens. Bioelectron.* **2013**, *43*, 461.
[11] M. Lu, Y. Qian, L. Huang, X. Xie, W. Huang, *ChemPlusChem* **2015**, *80*, 1216.
[12] X. Xie, Y. Cui Craig Criddle, *Energy Environ. Sci.* **2015**, *8*, 3418.
[13] T. H. Pham, P. Aelterman, W. Verstraete, *Trends Biotechnol.* **2009**, *27*, 168.
[14] A. Fraiwan, S. Sundermier, D. Han, A. Steckl, D. J. Hassett, S. Choi, *Fuel Cells* **2013**, *13*, 336.
[15] A. Fraiwan, S. P. Adusumilli, D. Han, A. J. Steckl, D. F. Call, C. R. Westgate, S. Choi, *Fuel Cells* **2014**, *14*, 801.
[16] S. Choi, H.-S. Lee, Y. Yang, P. Parameswaran, C. I. Torres, B. E. Rittmann, J. Chae, *Lab Chip* **2011**, *11*, 1110.
[17] M. Chiao, K. B. Lam, L. Lin, *J. Micromech. Microeng.* **2006**, *16*, 2547.
[18] H. Hou, L. Li, Y. Cho, P. de Figueiredo, A. Han, *PLoS ONE* **2009**, *4*, e6570.
[19] H. Hou, L. Li, C. U. Ceylan, A. Haynes, J. Cope, H. H. Wilkinson, C. Erbay, P. de Figueiredo, A. Han, *Lab Chip* **2012**, *12*, 4151.
[20] A. Han, H. Hou, L. Li, H. S. Kim, P. de Figueiredo, *Trends Biotechnol.* **2013**, *31*, 225.
[21] Y. He, Q. Fu, Y. Pang, Q. Li, J. Li, X. Zhu, R. Lu, W. Sun, Q. Liao, U. Schroder, *iScience* **2021**, *24*, 102163.
[22] M. Ghasemi, W. R. W. Daud, S. H. A. Hassan, S. Oh, M. Ismail, M. Rahimnejad, J. Md Jahim, *J. Alloys Compd.* **2013**, *580*, 245.
[23] Y. Wang, H. Huang, B. Li, W. Li, *J. Mater. Chem. A.* **2015**, *3*, 5110.
[24] W. Chen, Y. Huang, D. Li, H. Yu, L. Yan, *RSC Adv.* **2014**, *4*, 21619.
[25] X. Xie, L. Hu, M. Pasta, G. F. Wells, D. Kong, C. S. Criddle, Y. Cui, *Nano Lett.* **2011**, *11*, 291.
[26] X. Xie, M. Ye, L. Hu, N. Liu, J. R. McDonough, W. Chen, H. N. Alshareef, C. S. Criddle, Y. Cui, *Energy Environ. Sci.* **2012**, *5*, 5265.
[27] A. Baudler, I. Schmidt, M. Langner, A. Greiner, U. Schröder, *Energy Environ. Sci.* **2015**, *8*, 2048.
[28] M. Rezaie, S. Choi, *Small* **2023**, *19*, 2301125.
[29] M. Rezaie, Z. Rafiee, S. Choi, *Adv. Sustainable Syst.* **2024**, *8*, 2300357.
[30] F. O. Al-Qwiri, S. S. Shah, A. H. Shabi, A. Khan, M. A. Aziz, *Chem. Asian J.* **2024**, *19*, e202400314.
[31] S. F. Ketep, A. Bergel, A. Calmet, B. Erable, *Energy Environ. Sci.* **2014**, *7*, 1633.
[32] D. Pocaznoi, A. Calmet, L. Etcheverry, B. Erable, A. Bergel, *Energy Environ. Sci.* **2012**, *5*, 9645.
[33] C. Zitelli, P. Folgarait, A. Di Schino, *Metals* **2019**, *9*, 731.
[34] P. Nyamekye, P. Nieminen, M. R. Bilesan, E. Repo, H. Piili, A. Salminen, *Appl. Mater. Today* **2021**, *23*, 101040.
[35] N. Ulrich, K. Nagler, M. Laue, C. S. Cockell, P. Setlow, R. Moeller, *PLoS ONE* **2018**, *13*, e0208425.
[36] K. Kikuchi, L. Galer-Laporta, C. Weatherwax, J. Y. Lam, E. C. Moon, E. A. Theodorakis, J. Garcia-Ojalvo, G. M. Suel, *Science* **2022**, *378*, 43.
[37] L. M. Gonzalez, N. Mukhitov, C. A. Voigt, *Nat. Chem. Biol.* **2020**, *16*, 126.
[38] J. Ryu, S. Choi, *Biosens. Bioelectron.* **2021**, *186*, 113293.
[39] J. Ryu, M. Landers, S. Choi, *Biosens. Bioelectron.* **2022**, *205*, 114128.
[40] M. Landers, S. Choi, *Nano Energy* **2022**, *97*, 107227.
[41] K. Shahid, D. L. Ramasamy, S. Haapasaari, M. Sillanpaa, A. Pihlajamaki, *Energy* **2021**, *233*, 121213.
[42] A. A. Abbas, H. H. Farrag, E. El-Sawy, N. K. Allam, *J. Clea. Prod.* **2021**, *285*, 124816.
[43] K. A. Dwivedi, S. Huang, *Chem. Eng. J.* **2024**, *483*, 148871.
[44] T. Yamashita, Y. Yamashita, M. Takano, N. Sato, S. Nakano, H. Yokoyama, *Environ. Technol.* **2023**, *44*, 3229.
[45] P. Chong, B. Erable, A. Bergel, *Int. J. Hydrogen Energ.* **2019**, *44*, 4484.
[46] I. Yoda, H. Koseki, M. Tomita, T. Shida, H. Horiuchi, H. Sakoda, M. Osaki, *BMC Microbiol.* **2014**, *14*, 234.
[47] A. Khan, L. Xu, P. Kijkla, S. Kumseranee, S. Punpruk, T. Gu, *Bioelectrochemistry* **2024**, *159*, 108731.
[48] W. Steinhogi, G. Schindier, G. Steinlesberger, M. Traving, M. Engelhardt, *J. Appl. Phys.* **2005**, *97*, 023706.
[49] Z. Li, J. Wang, F. Li, Z. Li, E. Zhou, Y. Fan, H. Song, Z. Xu, T. Gu, F. Wang, D. Xu, *Angew. Chem. Int. Ed.* **2025**, *64*, e202425220.
[50] R. H. Mahmoud, O. M. Gomaa, R. Y. A. Hassan, *RSC Adv.* **2022**, *12*, 5749.
[51] M. Mohammadifar, S. Choi, *Adv. Mater. Technol.* **2017**, *2*, 1700127.
[52] Y. Liu, M. Ding, W. Ling, Y. Yang, X. Zhou, B. Li, T. Chen, Y. Nie, M. Wang, B. Zeng, X. Li, H. Liu, B. Sun, H. Xu, J. Zhang, Y. Jiao, Y. Hou, H. Yang, S. Xiao, Q. Liu, X. He, W. Liao, Z. Jin, Y. Xie, B. Zhang, T. Li, X. Lu, J. Li, F. Zhang, X. Wu, et al., *Energy Environ. Sci.* **2017**, *10*, 1600.
[53] J. You, R. J. Preen, L. Bull, J. Greenman, I. Ieropoulos, *Sustainable Energy Technol. Assess.* **2017**, *19*, 94.
[54] J. Yang, P. Xu, H. Li, H. Gao, S. Cheng, C. Shen, *ACS Appl. Bio Mater.* **2024**, *7*, 2734.
[55] D. P. E. Palmero, K. R. S. Pamintuan, *Int. J. Renewable Energy Dev.* **2023**, *12*.
[56] C. Reyes, E. Fivaz, Z. Sajo, A. Schneider, G. Siqueira, J. Ribera, A. Poulin, F. Schwarze, G. Nyström, *ACS Sustainable Chem. Eng.* **2024**, *12*, 16001.
[57] Y. M. Mao, K. Amreen, S. Goel, *IEEE Trans. NanoBiosci.* **2024**, *23*, 491.
[58] U. S. Jayapiriya, S. Goel, *Sustainable Energy Technol. Assess.* **2021**, *47*, 101535.
[59] J. An, J. Sim, Y. Feng, H. Lee, *Bioresour. Technol.* **2016**, *203*, 280.
[60] B. Kim, S. V. Mohan, D. Fapyane, I. S. Chang, *Trends Biotechnol.* **2020**, *38*, 667.
[61] S. Choi, J. Chae, *Sens. Actuators, A* **2012**, *177*, 10.